Int. J. Heat Mass Transfer. Vol. 36, No. 14, pp. 3529–3540, 1993
Printed in Great Britain

0017–9310/93 $6.00+0.00

CW laser machining of hard ceramics—II. Effects of multiple reflections

SE YOON BANG,† SUBHRANSU ROY‡ and MICHAEL F. MODEST
Department of Mechanical Engineering, The Pennsylvania State University, University Park, PA 16802, U.S.A.

(*Received* 7 *July* 1992 *and in final form* 27 *January* 1993)

Abstract—Beam guiding effects during laser machining of ceramics due to multiple reflections in the groove are analyzed theoretically for two extreme cases—purely specular and purely diffuse reflections. Specular reflections are valid for materials that have a smooth surface during laser evaporation (small optical roughness as compared to the laser wavelength). For such cases the material surface is divided into a number of rectangular patches using a bicubic surface representation method. The net radiative flux for these patch elements is obtained by ray tracing methods. The resulting radiative flux due to specular reflections is combined with the three-dimensional conduction equation governing conduction losses into the medium, and the resulting groove shape and depth are found through an iterative procedure. Diffuse reflections are valid for materials that have a very rough surface during material removal. To address beam coupling due to diffuse reflections, irradiation calculations employing view factor theory were combined with the three-dimensional conduction model. Considering multiple reflections results in an increased effective absorptivity and deeper grooves, accompanied by a flatter profile near the centerline and steeper slopes in the other parts of the groove cross-section. For the tested set of parameters, material removal rates are increased by up to 40% by specular reflections, and up to 70% by diffuse reflections. Experiments with hot-pressed silicon nitride ceramic showed increased beam coupling for deeper grooves (high power and/or slow scanning speeds) as predicted by considering multiple reflections. The agreement between theoretical calculations and experimental data for material removal rate and groove shape was good, if multiple reflections were assumed to be diffuse.

1. INTRODUCTION

LASERS have a variety of applications in modern technology because of their ability to produce high-power beams. Applications include welding, drilling, cutting, machining, medical surgery, and others. While considerable theoretical research has been done on laser welding and melt pool behavior [1] few theoretical studies have been done on laser machining or shaping. Laser cutting or shaping with a moving laser has been modeled by Modest *et al.* [2–5], and an extensive literature survey on previous works related to the present topic has been given by Bang and Modest [5]. Although the methodology of incorporating diffuse or specular reflections is well established in standard radiation problems, it has not been applied extensively to laser related processes. Baily and Modak [6] used the Monte Carlo method to simulate laser ablation with cavity reflections. To reduce statistical scatter of the Monte Carlo method and still conserve power, they used Legendre polynomial smoothing. They reported that ignoring multiple reflections may give discrepancies of up to 30% in predicted results. Minamida *et al.* [7] used the multiple reflection effects of high-power CO_2 laser beams for wedge shape welding and developed a simple simulation model using the ray tracing method. They achieved good prediction of the temperature profile in the sample. Bang and Modest [5] considered diffuse reflection effects on evaporative cutting using standard view factor theory with a quasi-one-dimensional conduction model, showing that multiple reflections result in increased material removal rates and deeper grooves, accompanied by a flatter profile near the centerline and steeper slopes in the other parts of the groove. Their analysis was limited to bodies which have a rough surface during laser evaporation (e.g. micro-explosive removal, violent surface boiling, etc.).

The reflection behavior of the workpiece is an important parameter in laser machining. For a linear-polarized beam the orientation of the polarization vector has a strong impact on material removal rates [8, 9]. To avoid the unpredictability of linear-polarized beams for general-purpose cutting, circularly polarized beams are generally used. Incidence angle dependence of absorptivity leads to high reflectivity for large off-normal incidence, especially in metals, resulting in deep penetration during cutting or welding. The angular dependence of absorptivity is also used for surface treatment to enhance the coupling rate using the high absorptivity at Brewster's angle for a linearly polarized beam [10, 11]. Multiple reflection and beam guiding effects become important for highly reflective materials or for deep grooves with

†Present address: Laser Applications Laboratory, Korean Institute of Machinery and Metals, Daejeon 305-301, Korea.
‡Present address: Center for Laser Technology, Indian Institute of Technology, Kanpur 208016, India.

NOMENCLATURE

F_0	radiation flux density at beam center at focal plane
$\mathbf{F}$	direct irradiation flux vector
h_{rc}	'heat of removal'
H, $\mathscr{H}$	total irradiation, dimensionless total irradiation
$\mathscr{H}_0$, $\mathscr{H}_s$	direct irradiation component, specular reflections component
k	thermal conductivity, absorption coefficient
m	complex index of refraction
n	index of refraction
$\hat{\mathbf{n}}$	inward unit surface normal
N_e	evaporation-to-laser power parameter
N_k	conduction-to-laser power parameter
N_z	beam divergence parameter
N_w	beam focusing parameter
P	laser power
s, S	groove depth
s_∞, S_∞	fully developed groove shape
$\hat{\mathbf{s}}$, $\hat{\mathbf{s}}_0$	unit direction vector for laser beam
T_{ev}, T_∞	evaporation temperature, ambient temperature
u	laser scanning speed
U	laser speed-to-diffusion parameter
v_n	transient surface recession normal to surface
w_0	effective radius of laser beam at focal plane
$w(z)$	laser beam radius at z
x, y, z	Cartesian coordinates.

Greek symbols

α_H	thermal diffusivity
$\alpha(x, y)$	local effective absorptivity at laser wavelength
θ	nondimensional temperature
ρ	density of the medium
ρ^s, ρ^d	specular reflectivity, diffuse reflectivity
ξ, η, ζ	nondimensional x, y, z coordinates
∇	$=\hat{\mathbf{i}}\partial/\partial x+\hat{\mathbf{j}}\partial/\partial y+\hat{\mathbf{k}}\partial/\partial z$.

aspect ratios greater than one, where large off-normal incidence causes high reflectivity values. Wallace [12, 13] found in his experiments that many grooves exhibited strongly-curved cross-sections that apparently resulted from beam guiding effects of partially polarized laser irradiation in the groove. Anthony [14] also concluded that the non-straight holes in his experiments resulted partly from 'beam channeling' due to reflections from side walls of the hole.

Actual reflection behavior depends on laser processing conditions, type of material, etc. In the present paper multiple reflections within the machined groove walls due to purely specular reflections are modeled and combined with the three-dimensional conduction model described in Part I of this study [4]. To study purely diffuse reflections, a previous diffuse reflection algorithm [5] is combined with the three-dimensional conduction model. Considering multiple reflections of the laser beam demonstrates how beam channeling increases the effective absorptivity of the material. To assess the applicability of multiple reflections models, theoretical predictions of groove size and material removal rates were compared with actual grooves cut in hot-pressed silicon nitride ceramic with single passes of a focussed CW laser beam at various power levels and scanning speeds.

2. THEORETICAL BACKGROUND

In order to obtain a realistic yet feasible mathematical description of the evaporation front in a moving solid subjected to a concentrated laser beam, several assumptions will be made [4]:

1. The solid moves with constant velocity u and the frame of reference is fixed to the laser.
2. The solid is isotropic with constant properties. Because the main emphasis of the present work is to study the effect of multiple reflections and beam guiding as compared to the three-dimensional model [4] where only direct irradiation is considered, this assumption is made to isolate beam guiding effects and to conserve CPU time (inclusion of variable properties necessitates much smaller time steps due to instability problems).
3. The material is opaque, i.e. the laser beam does not penetrate appreciably into the medium.
4. The change of phase from solid to vapor occurs in a single step at the evaporation temperature T_{ev}.
5. The evaporated material does not interfere with the incoming laser beam.
6. Heat losses by convection and radiation are negligible (as compared to conduction and change-of-phase losses).
7. At the surface, the laser beam is reflected in a fully specular fashion with reflectivity, ρ^s, obeying Fresnel's relationships. If a thin liquid zone is present, e.g. in the case of silicon nitride [13], and if the roughness of the layer is much less than the 10.6 μm wavelength of laser radiation, fairly specular behavior may be expected.

The reflectivity and absorptivity depend on a number of parameters, i.e. wavelength of the beam λ, temperature of the surface T, direction of incidence, etc. Since, for reflectivity variations, only the evaporation region is of interest, the temperature may be

assumed to be constant at the evaporation temperature T_{ev}. For laser cutting it is customary to use a circularly-polarized beam which essentially produces the same cut as an unpolarized beam. Hence, dependence on azimuthal angle of incidence will be neglected for the current study, and only the dependence on the polar incidence angle will be considered using Fresnel's relationships [15].

The laser beam is assumed to be in continuous-wave (CW) mode and to have a Gaussian power distribution with an effective radius $w(z)$, diverging away from the waist, given by Kogelnik and Li [16] as

$$w^2(z) = w_0^2 + \beta_\infty^2 (z_0 + z)^2; \quad \beta_\infty = \frac{\pi}{\lambda w_0}, \tag{1}$$

where w_0 is the effective radius at the focal plane (the waist) through which 86.5% (or $1-e^{-2}$) of the beam's energy passes, β_∞ is the far-field beam divergence angle, z_0 is the distance between the focal plane of the lens and the material surface ($z_0 > 0$ for focal point above surface, and $z_0 < 0$ for focal point below surface), and λ is the wavelength of the laser (cf. Fig. 1).

A Gaussian beam has a plane wave front at the waist (i.e. a radius of curvature of infinity) but assumes a curved wave front away from the beam waist. The radius of curvature of the wave front is:

$$r_c(z) = (z_0 + z)\left[1 + \frac{(w_0/\beta_\infty)^2}{(z_0+z)^2}\right]. \tag{2}$$

If the laser beam is visualized as consisting of a bundle of rays, then the ray direction is normal to the wave front surface having curvature $r_c(z)$. The direct radiation from the laser may then be expressed as:

$$\mathbf{F}(x, y, z) = \left[\frac{w_0^2}{w^2(z)}\right] F_0 e^{-2(x^2+y^2)/w^2(z)} \frac{\hat{\mathbf{s}}(x, y)}{\hat{\mathbf{s}} \cdot \hat{\mathbf{k}}}$$

$$\frac{\hat{\mathbf{s}}}{\hat{\mathbf{s}} \cdot \hat{\mathbf{k}}} = \frac{x\hat{\mathbf{i}} + y\hat{\mathbf{j}}}{\sqrt{(r_c^2(z) - x^2 - y^2)}} + \hat{\mathbf{k}}$$

$$= \tan\gamma \cos\phi \hat{\mathbf{i}} + \tan\gamma \sin\phi \hat{\mathbf{j}} + \hat{\mathbf{k}}, \tag{3}$$

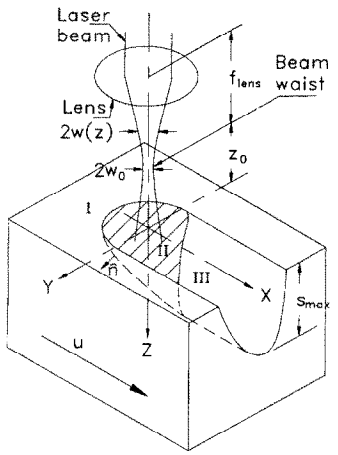

FIG. 1. Laser evaporation setup and coordinate system.

where γ is the angle between a laser ray and the z-axis, ϕ is the azimuthal angle for the ray measured from the x-axis in the x–y plane, and F_0 is the flux density at the beam center at the focal plane.

Under the above conditions the heat transfer problem for constant properties is expressed in non-dimensional transient form as [4]:

$$\frac{\partial \theta}{\partial \tau} + U\frac{\partial \theta}{\partial \xi} = \frac{\partial^2 \theta}{\partial \xi^2} + \frac{\partial^2 \theta}{\partial \eta^2} + \frac{\partial^2 \theta}{\partial \zeta^2}; \tag{4}$$

$$\xi \to \pm\infty, \quad \eta \to \pm\infty, \quad \zeta \to +\infty : \theta = 0; \tag{5a}$$

$\zeta = S(\xi, \eta)$:

$$\alpha \mathscr{H}(\xi, \eta) = -N_k \hat{\mathbf{n}} \cdot \nabla\theta + (V_n - U\hat{\mathbf{i}} \cdot \hat{\mathbf{n}})\frac{N_e}{U}. \tag{5b}$$

Boundary condition (5b) states that the absorbed total laser irradiation is partially converted into conduction losses and partially used for evaporation of material, if present (if no evaporation takes place, $V_n - U\hat{\mathbf{i}} \cdot \hat{\mathbf{n}} = 0$). At quasi-steady state, the transient recession in the direction normal to the surface, V_n, is zero and the energy expended for steady state evaporation is $-N_e(\hat{\mathbf{i}} \cdot \hat{\mathbf{n}})$ with $\hat{\mathbf{i}} \cdot \hat{\mathbf{n}} < 0$ wherever evaporation takes place.

To determine the groove shape, one more relation is needed:

$$\theta = 1, \quad \text{if} \quad V_n - U\hat{\mathbf{i}} \cdot \hat{\mathbf{n}} > 0 \tag{6}$$

stating that, during evaporation, the surface is at evaporation temperature. The non-dimensional variables are related to dimensional ones by

$$\xi = \sqrt{2}x/w_0, \quad \eta = \sqrt{2}y/w_0, \quad \zeta = \sqrt{2}z/w_0$$

$$\tau = 2\alpha_H t/w_0^2; \tag{7a}$$

$$S = \frac{\sqrt{2}s(x, y)}{w_0}, \quad \theta = \frac{T - T_\infty}{T_{ev} - T_\infty}, \quad \mathscr{H} = \frac{H(x, y)}{F_0}; \tag{7b}$$

$$N_e = \frac{\rho u h_{re}}{F_0}, \quad N_k = \frac{\sqrt{2}k(T_{ev} - T_\infty)}{F_0 w_0}, \quad U = \frac{u w_0}{\alpha_H \sqrt{2}},$$

$$V_n = \frac{v_n w_0}{\alpha_H \sqrt{2}}. \tag{7c}$$

Here ρ is the density of the medium, c its specific heat, k its thermal conductivity, $\alpha_H = k/(\rho c)$ is the thermal diffusivity, h_{re} its heat of removal (i.e. the energy required to remove an amount of solid, either by melting followed by evaporation, by sublimation, by partial evaporation combined with micro-explosive removal of particulates or some other mechanism), $s(x, y)$ is the local groove depth, and $\alpha(x, y) = 1 - \rho^s(x, y)$ is the local absorptivity. Physically, N_e gives the ratio of power required to evaporate material normal to the irradiation, and absorbed laser flux; N_k approximates the ratio of conduction losses, again for a surface normal to irradiation, and absorbed laser flux; U

relates the laser scanning speed to that of thermal diffusion (α_H) into the medium. Finally, V_n represents the transient recession of the evaporating surface with respect to the laser. The factor $\sqrt{2}$ appears in some of the dimensionless groups because $w_0/\sqrt{2}$ (i.e. the 1/e-radius of a Gaussian beam), has been chosen as a characteristic length scale in order to be consistent with previous works of the authors.

The total irradiation at a point on the groove surface may be determined from:

$$\mathscr{H}(\xi,\eta) = \mathscr{H}_0(\xi,\eta)+\mathscr{H}_s(\xi,\eta),$$

$$\mathscr{H}_0(\xi,\eta) = \mathbf{F}\cdot\hat{\mathbf{n}}/F_0 \quad (8)$$

where $\mathscr{H}_0$ is the dimensionless direct irradiation, and $\mathscr{H}_s$ is the contribution of specular reflections from the groove. Equation (4) with its boundary conditions (5a), (5b), (6) and (8) forms a complete set of dimensionless equations in transient form for the solution of the groove shape $S(\xi, \eta)$ and temperature field $\theta(\xi, \eta, \zeta)$.

3. SOLUTION APPROACH

The current problem requires an analysis with specular reflections between curved surfaces. The problem is further complicated by strong coupling between beam guiding and groove shape: the nature of beam-guiding has a strong influence on the shape of the hole or the groove that is being formed; this shape, in turn, has a strong influence on beam-guiding. Therefore, this difficult radiation problem must be solved iteratively together with the 3-D conduction problem. While such radiation problems are, in general, readily solved using the Monte Carlo technique, its use is problematic here. The 3-D temperature field turns out to be extremely sensitive towards the slightest variations in cavity shape, while the statistical scatter from the Monte Carlo method will always cause slight cavity variations from iteration to iteration. Therefore, ray tracing with non-random emission positions has been used in the current study.

Although the laser beam has a Gaussian intensity distribution and is best described by the wave equation [17], it may also be approximated as rays. The reflected direct irradiation is also assumed to consist of rays traveling along a straight path, i.e. the near-field phase information from wave theory is neglected. The total irradiation on the groove surface is then obtained by adding the direct irradiation calculated using equation (3) and the irradiation from multiple reflections. Irradiation values at nodal points resulting from second- or higher-order reflections are obtained from averaging irradiation values of surrounding elements by tracing a certain number of rays based on the amount of direct irradiation.

The reflected beam direction and the absorbed energy strongly depend on the surface normal and, therefore, on the method of surface representation. In the current study the groove surface is broken up into rectangular elements, and interior positions are expressed as bicubic interpolations of nodal values. Polynomials of high degree can describe complex curves, but they require a large number of coefficients whose physical significance is difficult to grasp and may also introduce unwanted oscillations in the curve. The cubics are found to be a good compromise in most applications. Ferguson [18] first introduced the use of parametric cubic equations for the definition of curves and surfaces in aircraft design. Segments of a curved line in space, described by third order polynomials in $u(0 \leqslant u \leqslant 1)$, may be expressed in terms of the position of the end points ($\mathbf{r}(0)$, $\mathbf{r}(1)$) and their first derivatives ($\mathbf{r}_u(0)$, $\mathbf{r}_u(1)$), i.e.

$$\mathbf{r} = \mathbf{r}(u) = \mathbf{r}(0)(1-3u^2+2u^3)+\mathbf{r}(1)(3u^2-2u^3)$$
$$+\mathbf{r}_u(0)(u-2u^2+u^3)+\mathbf{r}_u(1)(-u^2+u^3); \quad 0 \leqslant u \leqslant 1 \quad (9)$$

where,

$$\mathbf{r}(u) = x(u)\hat{\mathbf{i}}+y(u)\hat{\mathbf{j}}+z(u)\hat{\mathbf{k}}.$$

To obtain continuity across adjacent cubic segments, $\mathbf{r}$, $\mathbf{r}_u$ and $\mathbf{r}_{uu}$ are matched at the common points between adjacent segments (say 1 and 2).

$$\mathbf{r}_1(1) = \mathbf{r}_2(0), \quad \mathbf{r}_{u1}(1) = \mathbf{r}_{u2}(0), \quad \mathbf{r}_{uu1}(1) = \mathbf{r}_{uu2}(0). \quad (10)$$

The second derivatives are easily evaluated from (9), or

$$6\mathbf{r}_1(0)-6\mathbf{r}_1(1)+2\mathbf{r}_{u1}(0)+4\mathbf{r}_{u1}(1)$$
$$= -6\mathbf{r}_2(0)+6\mathbf{r}_2(1)-4\mathbf{r}_{u2}(0)-2\mathbf{r}_{u2}(1). \quad (11)$$

For a composite cubic curve through a set of points $\mathbf{r}_0, \mathbf{r}_1, \ldots, \mathbf{r}_n$, the above equation gives

$$\mathbf{r}_{ui-1}+4\mathbf{r}_{ui}+\mathbf{r}_{ui+1} = 3(\mathbf{r}_{i+1}-\mathbf{r}_{i-1}),$$
$$i = 1, 2, \ldots, n-1. \quad (12)$$

This is a recurrence relation between the slopes at three successive points. It is only necessary to specify $\mathbf{r}_{u0}$ and $\mathbf{r}_{un}$ to obtain a system of equations from which all the remaining slopes may be determined in terms of positional data alone.

To fit a surface the above definition of a curved line is extended by introducing a second parameter, v. Now the position vector $\mathbf{r}(u, v)$ is a function of two variables, u and v. A composite surface is built by joining surface patches, also known as Coon's patches, bound by four space curves: $(0, v)$, $(1, v)$, $(u, 0)$, and $(u, 1)$ (see Fig. 2(a)). A composite surface constructed on a curve network made up of cubic curves can be expressed as [19]:

$$\mathbf{r}(u,v) = UM\mathbf{Q}M^tV^t, \quad (13)$$

where

$$U = (1 \quad u \quad u^2 \quad u^3); \quad V = (1 \quad v \quad v^2 \quad v^3); \quad (14a)$$

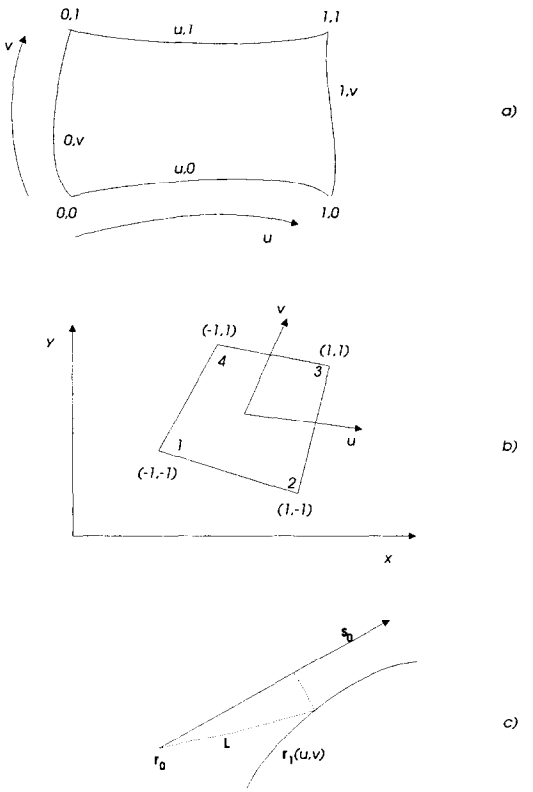

FIG. 2. Surface element representation and ray surface intersection. (a) Surface patch. (b) Isoparametric rectangular element (linear variation). (c) Distance from a point on the surface to a ray.

$$\mathbf{Q} = \begin{bmatrix} \mathbf{r}(0,0) & \mathbf{r}(0,1) & \mathbf{r}_v(0,0) & \mathbf{r}_v(0,1) \\ \mathbf{r}(1,0) & \mathbf{r}(1,1) & \mathbf{r}_v(1,0) & \mathbf{r}_v(1,1) \\ \mathbf{r}_u(0,0) & \mathbf{r}_u(0,1) & \mathbf{r}_{uv}(0,0) & \mathbf{r}_{uv}(0,1) \\ \mathbf{r}_u(1,0) & \mathbf{r}_u(1,1) & \mathbf{r}_{uv}(1,0) & \mathbf{r}_{uv}(1,1) \end{bmatrix};$$

$$M = \begin{bmatrix} 1 & 0 & 0 & 0 \\ 0 & 0 & 1 & 0 \\ -3 & 3 & -2 & -1 \\ 2 & -2 & 1 & 1 \end{bmatrix}. \quad (14b)$$

The 4×4 matrix $\mathbf{Q}$ is called a boundary matrix as it contains only geometrical properties from the boundary curves: corner coordinates, corner slopes, and corner twists. The corner twists, $\mathbf{r}_{uv}$ are all made equal to zero in the present application as in Ferguson's original papers. A notable application of this restricted type of patch appears in the APT surface-fitting routine FMILL [19] and NASA code by Craidon [20]. The blending function matrix M provides blending effects from one surface patch into an adjoining patch. Since the matrix product MQM^t is constant, the pre- and post-multiplications are performed and the equation is stored as $\mathbf{A} = MQM^t$ for further computer processing. The elements of $\mathbf{A}$ are, therefore, linear combinations of position and derivative vectors at the patch corners.

The quasi-Newton iteration method [21] is used to solve for the intersection of the ray with the bicubic surface. This has the computational advantage over the conventional Newton's method in that only first derivatives are required and no matrix inversion need to be done. The steps for finding the intersections between a ray and the parametric surface using this method have been well summarized by Joy and Bhetanabhotla [22] as follows. Given the parametric surface $\mathbf{r}(u, v) = [x(u, v), y(u, v), z(u, v)]$ and a ray, $\mathbf{r} = \mathbf{r}_0 + t\hat{\mathbf{s}}_0$, defined by the anchor $\mathbf{r}_0 = (x_0, y_0, z_0)$, and the unit direction $\hat{\mathbf{s}}_0 = (s_x, s_y, s_z)$, the square of the distance from the surface to the ray is obtained from (see Fig. 2(c)),

$$F(u,v) = |\mathbf{L}|^2 - (\mathbf{L}\cdot\hat{\mathbf{s}}_0)^2;$$

where,

$$\mathbf{L} = \mathbf{r}(u,v) - \mathbf{r}_0. \quad (15)$$

Rewriting, this becomes

$$F(u,v) = [x(u,v)-x_0]^2 + [y(u,v)-y_0]^2 + [z(u,v)-z_0]^2 - t^2, \quad (16)$$

where the distance along the ray to the point where the minimum $F(u, v)$ is achieved is given by

$$t = \mathbf{L}\cdot\hat{\mathbf{s}}_0 = s_x[x(u,v)-x_0] + s_y[y(u,v)-y_0] + s_z[z(u,v)-z_0]. \quad (17)$$

If a local minimum of F is zero, then this corresponds to a point where the ray intersects the surface. Those points where F is a minimum, but $F > 0$, indicate that the rays miss the surface by a finite distance. This is actually desirable in that the algorithm will still converge near 'silhouette edges' of surfaces, but will give a non-zero minimum.

When calculating the ray/surface intersections, the probability is high that two adjoining rays coming from the lens will strike the same surface, and will intersect the surface in the same general area. The same is true for adjoining reflected rays that hit the same surface. Therefore, in a large number of cases, the ray/surface intersection calculations should be nearly identical. If it can be determined that a ray potentially strikes a parametric surface $\mathbf{r}$, one can exploit ray coherence by setting the initial approximation $(u^{(0)}, v^{(0)})$ in the quasi-Newton iteration to be the parametric values (u, v) calculated on the final iteration by the quasi-Newton algorithm for the last ray to hit the surface.

For computational efficiency reasons, the patch is initially represented as a linear rectangular element, whose interior positions are expressed through linear interpolation of nodal values (cf. Fig. 2(b)),

$$x \approx \sum_{i=1}^{4} N_i x_i, \quad y \approx \sum_{i=1}^{4} N_i y_i, \quad z \approx \sum_{i=1}^{4} N_i z_i, \quad (18)$$

where the interpolation functions [23] are expressed as:

$$N_1 = \tfrac{1}{4}(1-u)(1+v), \quad N_2 = \tfrac{1}{4}(1+u)(1+v),$$
$$N_3 = \tfrac{1}{4}(1+u)(1-v), \quad N_4 = \tfrac{1}{4}(1-u)(1-v),$$
$$-1 \leqslant u \leqslant 1, \quad -1 \leqslant v \leqslant 1. \tag{19}$$

The approximate intersection point is calculated between this linear patch and a ray, providing a criterion to decide whether the more CPU-intensive bicubic patch representation, described earlier, is needed to get a correct intersection point. The intersection point between such linear patch and the ray $\mathbf{r}_0 + t\hat{\mathbf{s}}_0$ is obtained by solving

$$\mathbf{r}(u, v) = [x(u, v), y(u, v), z(u, v)] = \mathbf{r}_0 + t\hat{\mathbf{s}}_0. \tag{20}$$

After algebraic manipulation one can obtain a quadratic equation for u or v. If either the solution for $|u|$ or for $|v|$ lies within the range $|u|, |v| < 1+\varepsilon$, or the distance from center (0, 0) of element to the ray is less than a small number, then the bicubic representation of that patch is used to find the correct intersection point between the ray and the patch.

The specular reflection term calculated from ray tracing is incorporated into the differential equations governing the groove shape by averaging over the subsurfaces surrounding a nodal point. The number of surface elements in most cases is about 600–900, requiring 4–5 h of CPU time on an IBM RS 6000/320H computer.

A first approximation of S (i.e. the groove shape) is obtained by neglecting multiple reflections while using the given absorptivity. Using this groove shape, the local irradiation due to specular reflections is calculated and added to the boundary condition of the conduction equation to update the groove shape. The governing equations and boundary conditions are extremely non-linear and very sensitive to the added reflected energy. This is especially true for deep grooves with high reflectivity. The transient three-dimensional conduction equation is finite-differenced for a grid system generated by the body-fitted coordinates method and solved by the approximate factorization scheme (alternate direction type) [4].

Diffuse reflection effects have already been addressed previously using a quasi-one-dimensional conduction model [5]. To address the contribution of diffuse reflections with three-dimensional conduction, the code used in the previous quasi-one-dimensional model is combined with the current three-dimensional conduction model. View factors for the rectangular patches are obtained from those for subdivided triangular elements using reciprocity and view factor algebra. Both contour integration and numerical quadrature of triangular elements are used to evaluate view factors.

4. DISCUSSION OF THEORETICAL RESULTS

To investigate the effects of multiple specular reflections, a parallel beam ($\beta \approx 0$ and $\hat{\mathbf{s}} = \hat{\mathbf{k}}$) laser with constant absorptivity ($\alpha = 0.3$) was used for most cases except when specified otherwise. The range of non-dimensional parameters, over which cutting of hard ceramics such as silicon nitride or silicon carbide with a CO_2 laser takes place, covers approximately $U \simeq 1$–50, $N_k \simeq 0.005$–0.05, and $N_c \simeq 0.04$–2 [24]. For comparison, results for grooves with diffusely-reflecting walls have been included for a number of cases, using the same 3-D conduction model. In the following discussion, the former is referred to as the '3-D diffuse model', and the present model as the '3-D specular model'.

Figure 3(a) shows a typical groove development along the ξ-direction and the final groove shape for the case of $U = 2$, $N_k = 0.05$, $N_c = 0.1$ corresponding to a case of relatively low laser power and scan velocity. At $\xi = +0.75$ evaporation still takes place while, without reflections, the final groove shape would have been reached. Grooves with diffuse reflections develop faster and deeper than those with specular reflections since the developing (i.e. evaporating) region can receive additional irradiation from downstream positions. The fully-developed groove cross-sections for both the 3-D specular and diffuse models have steeper groove walls with a flatter center region as compared with those without reflection effects. The groove predicted by the 3-D specular model is shallower and has an even flatter center region as compared with the 3-D diffuse model. This is clearly demonstrated in Fig. 3(b), which shows a top view of the contour lines of surface temperatures under the laser beam. Considering multiple reflections results in an extended evaporation zone with a different shape. Due to beam channeling from the upstream wall as well as the side walls, the evaporation zone extends farther downstream. Specular reflections result in an off-centered extension of the evaporation zone, while diffuse reflections extend the evaporation zone along the centerline.

Contour lines for the absorbed irradiation are depicted in Fig. 4 for absorbed total and multiply-reflected irradiation, normalized by their maximum value. The maximum value of specular irradiation (i.e. without direct irradiation) is $\mathscr{H}_{s\max} = 0.09$ and larger than twice that of diffuse irradiation ($\mathscr{H}_{d\max} = 0.04$). Specularly reflected rays hit the side walls far downstream and increase the amount of energy absorbed there. The specularly reflected irradiation shows a more concentrated region with an off-centerline peak resulting in a similar peak for the total irradiation, which explains the off-centered extension of the evaporation zone. The diffusely-reflected irradiation shows a smooth variation giving a smooth profile for total irradiation and an extension of the evaporation zone along the centerline.

For moderately deep grooves with $U = 10$, $N_k = 0.01$, $N_c = 0.01$, corresponding to a case of high laser power and intermediate scanning velocity, the reflection pattern shown in Fig. 5(a) is quite different as compared with the low power/low speed case,

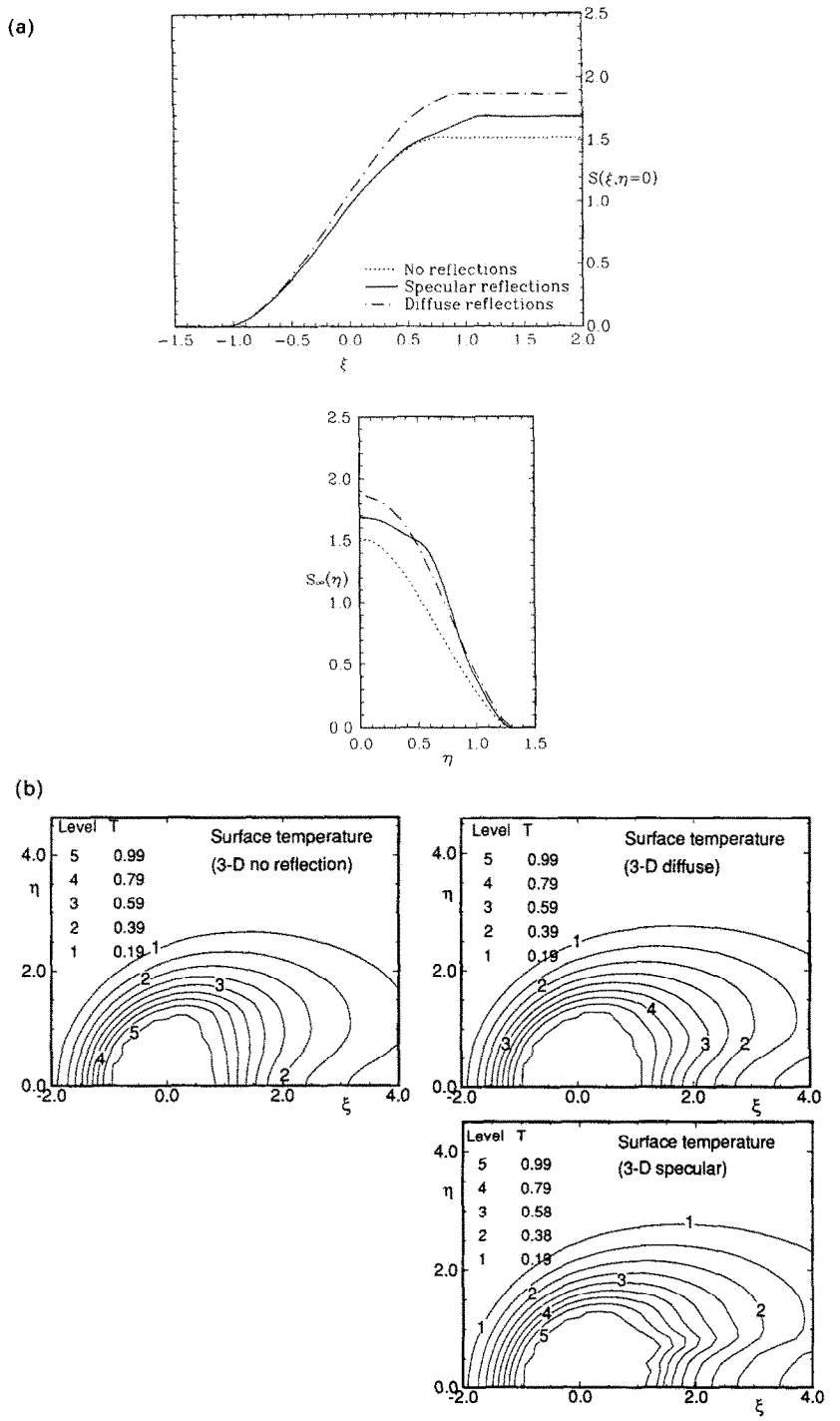

FIG. 3. Laser grooving for $U = 2$, $N_k = 0.05$, $N_c = 0.1$, parallel beam, $\alpha = 0.3$—effect of specular, diffuse and no reflection. (a) Groove cross-section along centerline and final groove shape. (b) Surface temperature profiles.

shown in Fig. 4. Two peaks are found on each side of the groove for specularly reflected irradiation, causing an extended evaporation zone along the centerline. Figure 5(b) depicts the same situation for diffuse reflections. The diffuse model, as expected, predicts a smoothly-varying reflection profile with a mild peak on each side wall, resulting in a smoothly-extended profile of absorbed total irradiation and the evaporation zone. The maximum values of total irradiation for both specular and diffuse cases are nearly the same. However, the maximum of specular irradiation is ~50% of the total irradiation while that

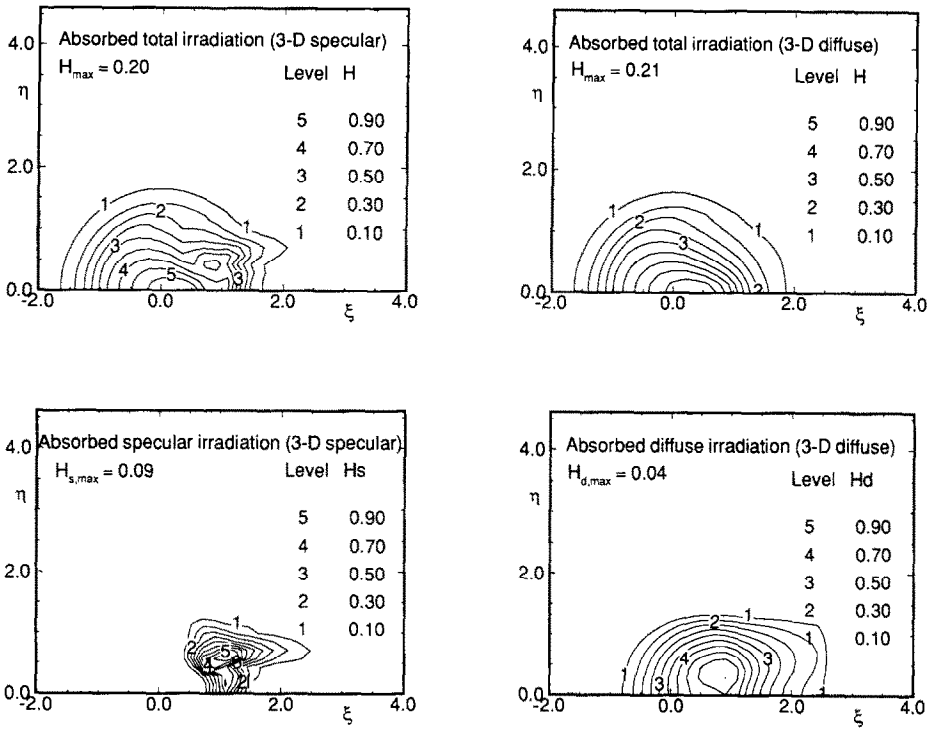

FIG. 4. Laser grooving for $U = 2$, $N_k = 0.05$, $N_e = 0.1$, parallel beam, $\alpha = 0.3$—effect of specular and diffuse reflection on irradiation profiles.

of diffuse irradiation is only ~35%. Figure 6 shows the corresponding groove shapes along the centerline and the final groove cross-sections. Up to $\xi = 0.6$–0.7 there is no additional irradiation in a specularly reflecting groove and the shapes with and without reflections remain the same. For larger ξ, multiple specular reflections start to carve out the bottom of the grooves, resulting in steeper grooves, which have more uniform kerf width. The second peak found in the reflection plot (at $\xi \simeq 2.0$) helps forming the additional second hump in groove depth along the centerline. The groove shape for the same parameters for diffuse reflections is also shown in the same plot. Although the cross-sectional shape is similar to that of the 3-D specular model, the final groove depth for the 3-D diffuse model becomes deeper, indicating that diffuse reflections trap radiation more effectively. The effective absorptivity is increased by 30% with the 3-D specular model, while a 48% increase is observed with the 3-D diffuse model.

The influence of absorptivity α on the importance of specular and diffuse reflections is shown in Fig. 7(a). Here $U = 10$, $N_k = 0.01$, and $N_e = 0.01$ have again been selected as representative values. Similar to the results with diffuse reflections, the specular reflection model predicts a significant increase in groove depth and the formation of different groove shapes compared with the case without reflections. For intermediate values of α, the reflections from the wall produce a wider flat-center region and steeper groove walls. By comparing material removal rates with and without beam guiding (see Bang and Modest [5]), one can calculate an 'effective absorptivity' for each case, showing that the effect of beam-guiding is reduced as α increases, and, of course, the groove shapes become identical for $\alpha = 1$. For the current parameters, the effective absorptivity is increased by 10 to 33% if specular reflections are considered. Comparing material removal rates (Fig. 7(b)), it is found that both the diffuse and specular models show the same tendencies in material removal vs absorptivity/reflectivity, except that the increase is smaller for specular reflections.

The current model can incorporate the angular dependence of reflectivity, for which Fresnel's relationship for a circularly polarized beam is used (however, changes in the polarization after multiple reflections have been neglected). To investigate this effect, a complex index of refraction $m = 1.5$–$3.71i$ was selected. This value of m approximates solid Si_3N_4 near its decomposition temperature with $\alpha = 0.3$ at normal incidence (see Ramanathan and Modest [24]). The hemispherical absorptivity turns out to be 0.305, and a significant increase in reflectivity occurs for incidence angles larger than 75°. The groove shape for the case of $U = 10$, $N_k = 0.01$, and $N_e = 0.01$ is depicted in Fig. 8. The results for specular reflections with both diffuse absorption ($\alpha = 0.3$, $\rho^s = 0.7$) and Fresnel absorption [$\rho^s = \rho^s(\theta)$, $\alpha = 1 - \rho^s$], are compared in the same plot. It is observed that the case of Fresnel reflection results in a similar groove profile as the case of diffuse absorptivity, with a slightly increased

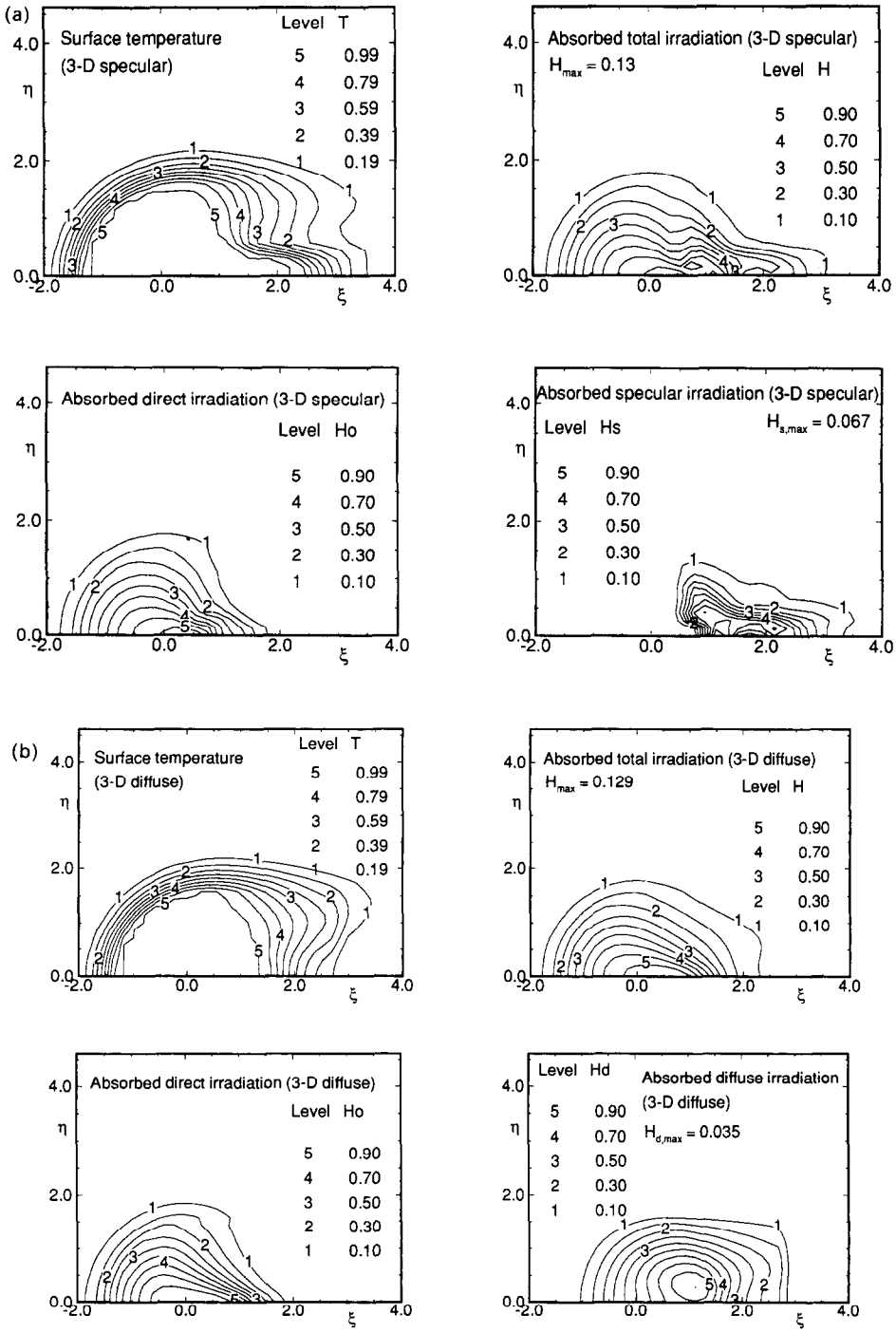

FIG. 5. Laser grooving at $U = 10$, $N_k = 0.01$, $N_c = 0.01$, parallel beam, $\alpha = 0.3$—effect of (a) specular and (b) diffuse reflections on temperature and irradiation profiles.

maximum groove depth, apparently due to the slightly higher hemispherical absorption. Overall, the effects of the absorptivity variation due to different incidence angles are rather minor since the important reflections from the front wall of the groove have incidence angles less than 75° (for which the absorptivity is almost diffuse) and those from the side walls are, apparently, unimportant.

5. DISCUSSION OF EXPERIMENTAL RESULTS

Hot-pressed silicon nitride (Si_3N_4) ceramic was machined with a 1500 W CO_2 laser, model Everlase S51, manufactured by Coherent General. Grooves were made with a single scan of the laser beam focussed on the surface. Several grooves were cut at various power levels (600, 1100 and 1500 W) and

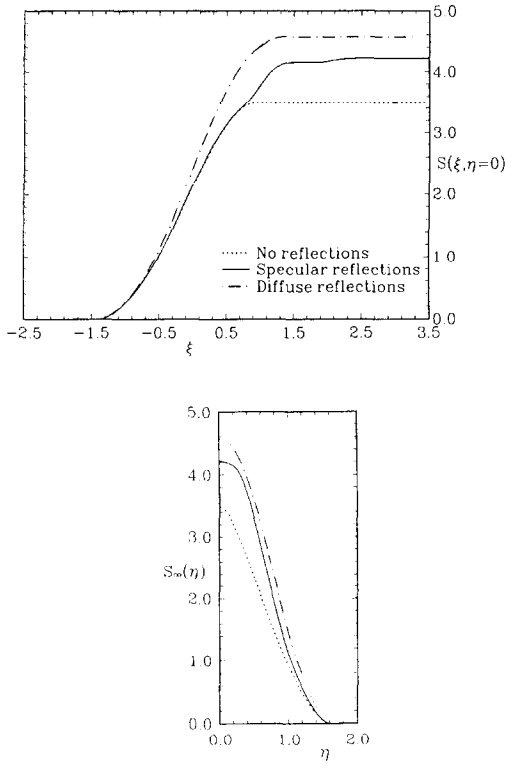

FIG. 6. Laser grooving for $U = 10$, $N_k = 0.01$, $N_e = 0.01$, parallel beam, $\alpha = 0.3$—effect of specular, diffuse and no reflections on groove shape.

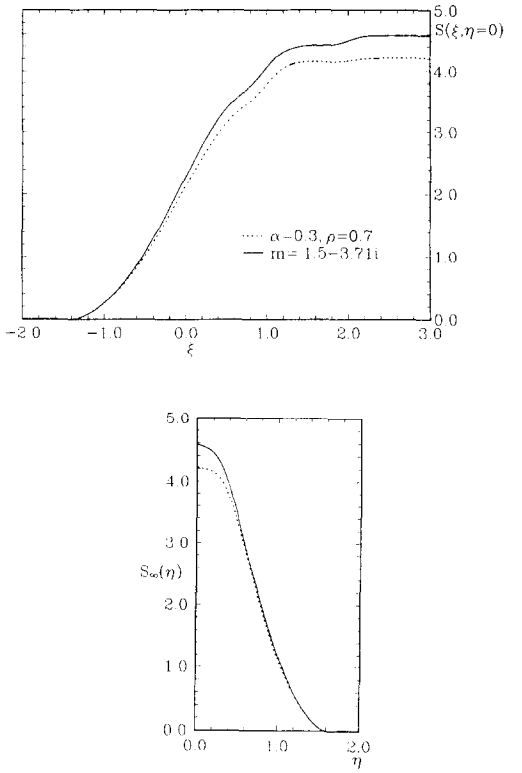

FIG. 8. Groove shapes for specular reflections obeying Fresnel's law ($U = 10$, $N_k = 0.01$, $N_e = 0.01$, parallel beam).

speeds (5, 10 and 20 cm s $^{-1}$). The samples were sectioned with a diamond blade perpendicular to the scanning direction. Scanning electron microscope (SEM) pictures of groove cross-section on the two cut surfaces were digitized resulting in two sets of groove cross-section data for each groove. The experimental results were compared with theoretical calculations for two extreme cases of multiple reflections—fully specular and fully diffuse. The evaluation of thermophysical properties for silicon nitride and the cutting parameters are explained in a companion paper [4] and are summarized in Table 1. Constant material properties (evaluated at decomposition/evaporation temperature) were used in the calculations.

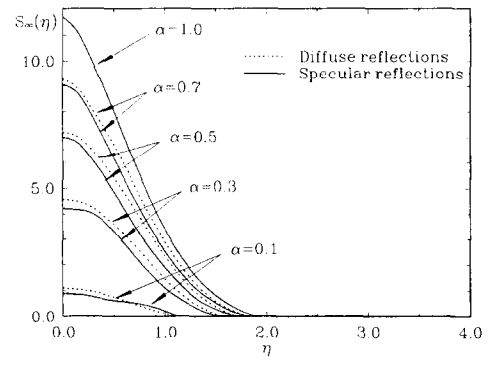

FIG. 7. Laser grooving for $U = 10$, $N_k = 0.01$, $N_e = 0.01$, parallel beam—effect of absorptivity on (a) groove depth and (b) material removal rate.

During laser machining, Si_3N_4 decomposes into liquid silicon and gaseous nitrogen [25],

$$Si_3N_4(s) \rightarrow 3Si(l) + 2N_2(g).$$

The production of subsurface nitrogen at a pressure greater than 0.1 MPa causes the silicon liquid layer to rupture and be ejected. The absorptivity in the evaporation zone was estimated by considering that the surface where decomposition takes place is at least partially covered with a thin layer of liquid silicon. The reflectivity of molten silicon at the CO_2 laser wavelength can be calculated from its complex refractive index ($m = n - ik = 19.6 - 20.4i$) [26]. The absorptive index, k, for liquid silicon is so high that even a thin film of liquid silicon (say, 1 μm) is optically opaque, and therefore the reflectivity of the interface between the liquid silicon film and the solid, silicon

Table 1. Property values and cutting parameters for Si_3N_4

T_{ev}	2151 K	h_{re}	6206 kJ kg^{-1}
k	12.14 W m^{-1} K^{-1}	α	0.15
ρ	3250 kg m^{-3}	α_0	1.0
c	1294.5 J kg^{-1} K^{-1}	w_0	212 μm

nitride, need not be accounted for. Absorptivities of solid silicon nitride were measured at various temperatures [27] and were extrapolated to be approximately 0.3 near the decomposition temperature. Since the decomposition-front surface is expected to be only partially covered with a liquid silicon film through which nitrogen is escaping, the actual local absorptivity should be in the range $0.1 < \alpha < 0.3$. An average absorptivity of 0.15 was used for the evaporating surface since this value gave best agreement between theoretical and experimental shallow grooves for which beam guiding is insignificant [4].

The volume removal rates for silicon nitride at various powers and speeds, obtained from experiments as well as calculated by considering multiple reflections in the groove, are shown in Fig. 9. It is observed experimentally that there is a distinct rise in material removal rate at lower speeds when grooves are deep. Apparently, such increase in material removal rate at lower speeds is due to better coupling between the laser and the groove surface. At lower speeds, as the groove becomes deeper, beams are trapped due to multiple reflections inside the groove, increasing the total absorption rate. From the graph it is seen that for shallow grooves (at low powers combined with fast scanning velocities) the effective absorptivity is about 15%. For shallow grooves beam trapping due to diffuse reflections is very small and beam trapping due to specular reflections is non-existent. However, at higher powers the effective absorptivity could be as high as 25% for the data shown. How much of that is due to specular reflections and how much is due to diffuse reflections is not known. For a laser power of 1100 W, the increase in material removal rate, for the deepest groove cut at the lowest speed, as predicted by specular reflections is only 25%, while the experimentally observed increase is about 60% as shown in Fig. 9. Considering diffuse reflections predicts somewhat higher removal rates but still falls on the lower side of the experimentally observed data band. Therefore, there seems to be an increase in the effective utilization of the laser power by some other unexplained phenomenon. The roughness of the surface due to undulations in the silicon layer and voids in the liquid layer caused by the ejected nitrogen gas is seen differently depending on the angle with which the laser beam strikes the layer. The increase in roughness perceived by the laser beam for steeper and deeper grooves at lower speeds can explain the increase in removal rate at lower speeds and higher powers over and above that predicted by multiple reflections.

While examination of the material removal rate gives an overall idea of the removal process from the heat transfer point of view, the shape of the grooves as predicted from theory and from experiments gives additional insight into the material removal process. If internal reflections are neglected for deep grooves (see Fig. 10 for powers of 1100 and 1500 W), the theoretical groove cross-sections show strong taper at their bottom. Considering multiple reflections within the groove increases the depth of the groove and greatly changes the shape of the groove, widening it at the bottom; both effects cause an increase in the material removal rate. For deep grooves, a 15% absorptivity value predicts the material removal rate rather accurately if diffuse reflections inside the groove are accounted for. If variable thermophysical properties are considered the predicted material removal rates will drop by 5–15%, but the trends in variation of

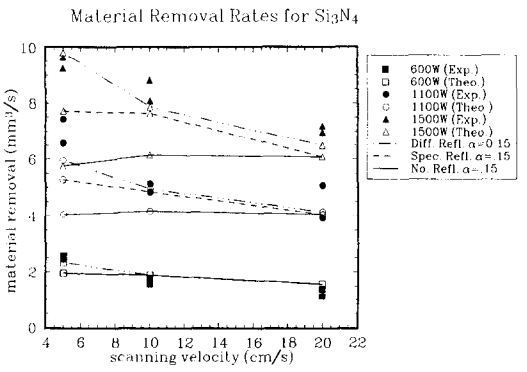

FIG. 9. Material removal rate during laser grooving considering multiple reflections.

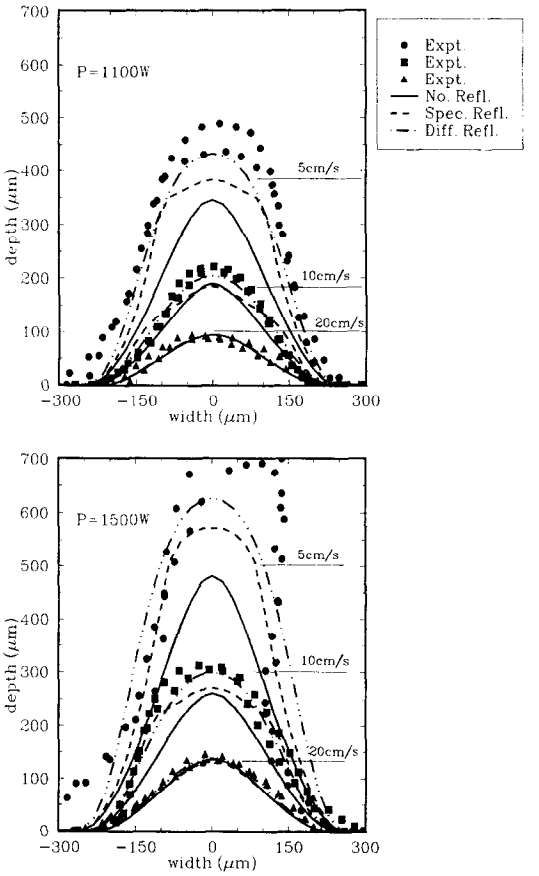

FIG. 10. Groove cross-section at 1100 and 1500 W power and different scanning speeds.

material removal rates with laser scanning speed and power will be predicted best by considering diffuse reflections. Considering the uncertainties in radiative properties in the decomposition front the agreement between theoretical predictions and experimental data is very good.

6. SUMMARY

Multiple specular reflections and beam guiding effects on evaporative cutting with a CW laser have been investigated. Irradiation calculations using ray tracing with bicubic surface patches have been combined with a transient three-dimensional conduction model. It was found that beam guiding plays an important role in forming the fully-developed groove, resulting in an increased effective absorptivity.

Due to beam channeling from the upstream wall as well as the side walls, the specularly-reflected irradiation produces a strong peak far downstream, thus extending the evaporation zone, while diffusely reflected irradiation shows a smooth variation with a mild peak. Multiple specular reflections also produce flatter profiles near the centerline and steeper slopes in the other parts of the groove cross-sections, and similar behavior is observed for diffuse reflections. The effective absorptivity is increased by 15–30% for the set of parameters in the current 3-D specular reflection model, while the 3-D diffuse reflections produce an increase of up to 50–70% for the same set of parameters. Generally, specular and diffuse beam guiding effects become significant for high-reflectivity materials and/or deep groove cases. For deep grooves cut in silicon nitride the beam guiding models predict an increase in material removal rate and groove size at lower speeds consistent with the experimental observations. For silicon nitride the diffuse reflection model gives better agreement between theoretical predictions and experimental data.

Acknowledgement—Support for this work by National Science Foundation Grant CTS-8915027 is gratefully acknowledged.

REFERENCES

1. J. Mazumder, An overview of transport phenomena in laser materials processing. In *International Conference on Laser Advanced Materials Processing—Science and Applications*, Osaka, Japan, pp. 613–624, High Temperature Society of Japan, Japan Laser Processing Society (1987).
2. M. F. Modest and H. Abakians, Evaporative cutting of a semi-infinite body with a moving CW laser, *J. Heat Transfer* **108**, 602–607 (1986).
3. S. Ramanathan and M. F. Modest, Single and multiple pass cutting of ceramics with a moving CW laser. In *Proceedings of the XXII ICHMT Intl. Symposium on Manufacturing and Materials Processing*, Dubrovnik, Yugoslavia (1990).
4. S. Roy and M. F. Modest, CW laser machining of hard ceramics—I. Effects of three-dimensional conduction and variable properties, *Int. J. Heat Mass Transfer* **36**, 3515–3528 (1993).
5. S. Y. Bang and M. F. Modest, Multiple reflection effects on evaporative cutting with a moving CW laser, *J. Heat Transfer* **113**(3), 663–669 (1991).
6. A. W. Baily and A. Modak, Numerical simulation of laser ablation with cavity reflections, *J. Thermophys. Heat Transfer* **3**(1), 42–45 (1989).
7. K. Minamida, H. Takafuji, N. Hamada, H. Haga and N. Mizuhashi, Wedge shape welding with multiple reflection effects of high power CO_2 laser beam. In *5th International Congress on Applications of Lasers and Electro-optics* (1986).
8. F. O. Olsen, Investigations in optimizing the laser cutting processes. In *Proc. Lasers in Materials Processing*, American Society of Materials (1983).
9. W. W. Duley, *Laser Processing and Analysis of Materials*. Plenum Press, New York (1983).
10. F. Dausinger and T. Rudlaff, Novel transformation hardening technique exploiting Brewster absorption. In *International Conference on Laser Advanced Materials Processing—Science and Applications*, Osaka, Japan, pp. 323–328, High Temperature Society of Japan, Japan Laser Processing Society (1987).
11. F. Dausinger, M. Beck, J. H. Lee, E. Meiners, T. Rudlaff and J. Shen, Energy coupling in surface treatment processes, *J. Laser Appl.* **2**(3–4), 17–21 (1990).
12. R. J. Wallace, A study of the shaping of hot pressed silicon nitride with a high power CO_2 laser, Ph.D. Thesis, University of Southern California, Los Angeles, CA (1983).
13. R. J. Wallace and S. M. Copley, Laser machining of silicon nitride: energetics, *Adv. Ceramic Mater.* **1**(3), 277–283 (1986).
14. T. R. Anthony, The random walk of a drilling laser beam, *J. Appl. Phys.* **51**, 1170–1175 (1980).
15. M. F. Modest, *Radiative Heat Transfer*. McGraw-Hill, New York (1993).
16. H. Kogelnik and T. Li, Laser beams and resonators, *Applied Optics* **5**(10), 1550–1565 (1956).
17. J. T. Verdeyen, *Laser Electronics*. Prentice-Hall, Englewood Cliffs, NJ (1981).
18. J. C. Ferguson, Multivariate curve interpolation, *Journal ACM* **11**(2), 221–228 (1964).
19. I. D. Faux and M. J. Pratt, *Computational Geometry for Design and Manufacture* (1st Edn). Ellis Horwood, Chichester, UK (1979).
20. C. B. Craidon, A computer program for fitting smooth surfaces to an aircraft configuration and other three-dimensional geometries, NASA TM X-3206 (1975).
21. *User's Manual: IMSL Math/Library* (1st Edn). IMSL, Houston, TX (1989).
22. K. I. Joy and M. N. Bhetanabhotla, Ray tracing parametric surface patches utilizing numerical techniques and ray coherence, *Computer Graphics* **20**(4), 279–284 (1986).
23. T. J. Chung, *Finite Element Analysis in Fluid Dynamics* (1st Edn). McGraw-Hill, New York (1978).
24. S. Ramanathan and M. F. Modest, Effect of variable properties on evaporative cutting with a moving CW laser. In *Heat Transfer in Space Systems*, Vol. HTD-135, ASME (1990).
25. S. C. Singhal, Thermodynamic analysis of the high-temperature stability of silicon nitride and silicon carbide, *Ceramurgia Int.* **2**, 123–130 (1976).
26. C. P. Grigoropoulos, Inhomogeneous melting of thin silicon films irradiated with CO_2 laser light, ASME Paper No. 91-HT-40 (July 1991).
27. S. Roy, S. Y. Bang, M. F. Modest and V. S. Stubican, Measurement of spectral, directional reflectivities of solids at high temperatures between 9 and 11 μm. In *Proceedings of the ASME/JSME Engineering Joint Conference*, Vol. 4 (1991).